

Robust AC vector sensing at zero magnetic field with pentacene

Boning Li,^{1,2,*} Garrett Heller,^{2,3,*} Jungbae Yoon,² Alexander Ungar,^{2,3} Hao Tang,⁴ Guoqing Wang,⁵ Patrick Hautle,⁶ Yifan Quan,⁷ and Paola Cappellaro^{1,2,8,†}

¹*Department of Physics, Massachusetts Institute of Technology, MA 02139, USA*

²*Research Laboratory of Electronics, Massachusetts Institute of Technology, Cambridge, MA 02139, USA*

³*Department of Electrical Engineering and Computer Science, Massachusetts Institute of Technology, MA 02139, USA*

⁴*Department of material science and engineering, Massachusetts Institute of Technology, Cambridge, MA 02139, USA*

⁵*Department of Physics, Peking University, Beijing, 100871, P.R.China*

⁶*Paul Scherrer Institute, 5232 Villigen, Switzerland*

⁷*Department of Chemistry, University of Pennsylvania, Philadelphia, PA 19104, USA*

⁸*Department of Nuclear Science and Engineering, Massachusetts Institute of Technology, Cambridge, MA 02139, USA*

Quantum sensors based on electronic spins have emerged as powerful probes of microwave-frequency fields. Among other solid-state platforms, spins in molecular crystals offer a range of advantages, from high spin density to functionalization via chemical tunability. Here, we demonstrate microwave vector magnetometry using the photoexcited spin triplet of pentacene molecules, operating at zero external magnetic field and room temperature. We achieve full three-dimensional microwave field reconstruction by detecting the Rabi frequencies of anisotropic spin-triplet transitions associated with two crystallographic orientations of pentacene in deuterated naphthalene crystals. We further introduce a phase alternated protocol that extends the rotating-frame coherence time by an order of magnitude and enables sensitivities of approximately $1 \mu\text{T}/\sqrt{\text{Hz}}$ with sub-micrometer spatial resolution. These results establish pentacene-based molecular spins as a practical and high-performance platform for microwave quantum sensing in addition to demonstrating control techniques broadly applicable to other molecular and solid-state spin systems.

I. INTRODUCTION

Quantum sensors based on optically-detected solid-state defect spin qubits have demonstrated remarkable sensitivity to electromagnetic fields [1–5], enabling nanoscale imaging and precision metrology for spin-wave imaging [6, 7], micro-electronic device characterization [8, 9], and bio-sensing [10, 11]. Despite these advances, defect-based quantum sensors face intrinsic limitations. Their scalability is constrained by the difficulty of creating high-density, uniform defect ensembles, as the accompanying increase in surrounding spin impurities leads to decoherence [12–15]. Furthermore, at low external magnetic fields, inhomogeneous charge and strain environments mix the spin energy levels, degrading both the coherence and the sensing accuracy [16].

Molecular quantum systems [17, 18] with optically addressable spin degrees of freedom have recently emerged as a compelling alternative route for quantum sensing [19–22]. These molecular spins can exhibit long coherence times and combine the advantages of chemically programmable spin sites with high density doping in many host crystals [23, 24]. These properties allow molecular color centers to operate under conditions where conventional solid-state defect qubits typically fail, such as in flexible substrates or amorphous environments [25].

Optical addressability further enables efficient initialization and read-out of spin states.

Among these systems, *pentacene* stands out for its long-lived photoexcited triplet states and efficient optical spin polarization at room temperature [17–20]. As an organic molecule, pentacene can be incorporated into thin films [26, 27], patterned directly on chip [28], or grown as bulk crystals, offering versatility for device integration and scalable sensing architectures.

Here, leveraging an ensemble of photoexcited triplet states of pentacene molecules embedded in a naphthalene single crystal, we develop a Rabi-based protocol that exploits the intrinsic multi-orientational structure and anisotropic spin transitions for vector AC magnetic-field sensing at microwave frequencies. To further enhance its sensitivity, we introduce a phase-modulated control scheme [29–31] that effectively decouples the qubit from field fluctuations and inhomogeneities that arise from the environment and the driving itself. With this approach, we demonstrate magnetic-field sensitivities reaching $1 \mu\text{T}/\sqrt{\text{Hz}}$ under ambient conditions with sub-micrometer spatial resolution. Overall, these results establish a viable pathway toward room-temperature quantum sensing and vector-field imaging using molecular spin systems.

* These authors contributed equally.

† pcappell@mit.edu

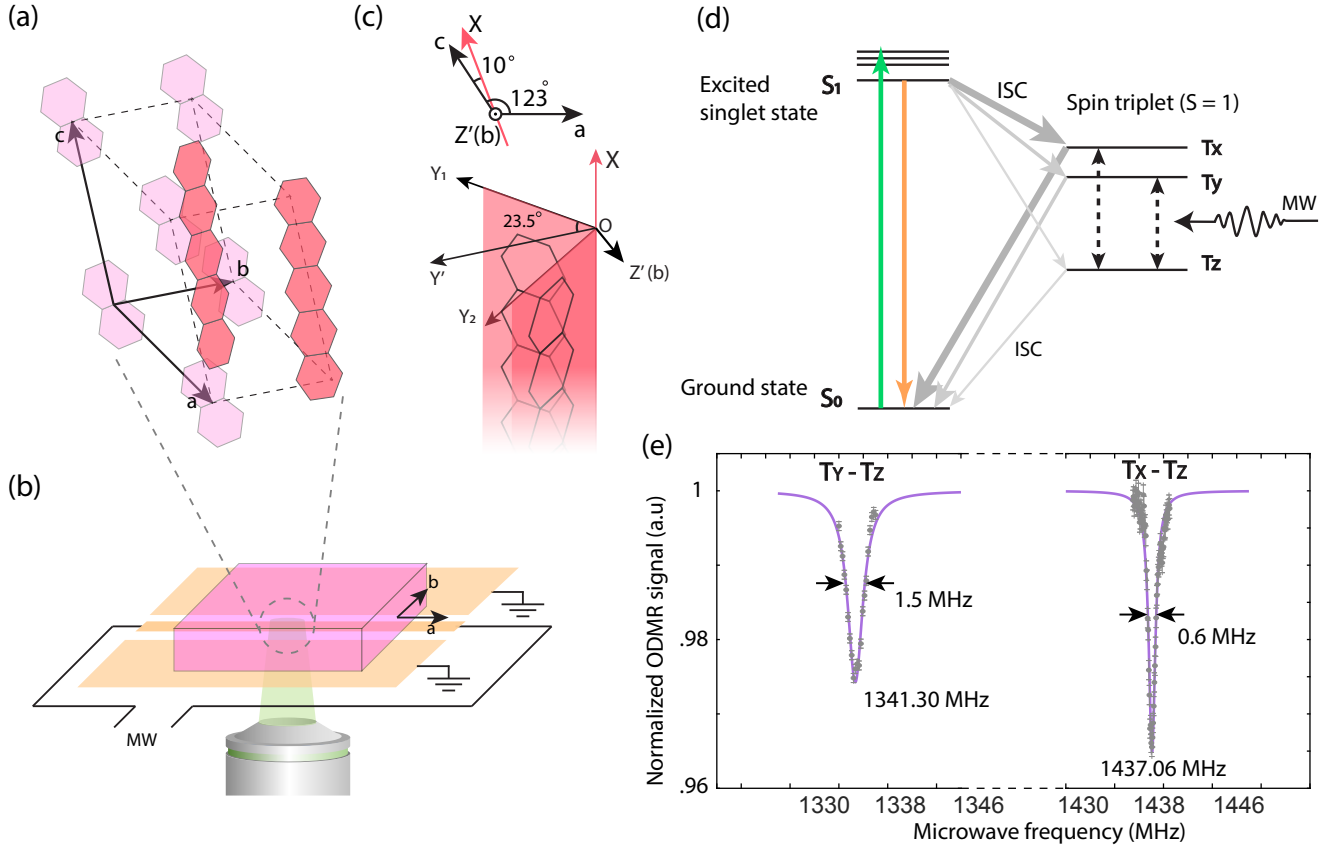


FIG. 1. **Experimental setup and pentacene properties.** (a) Crystal structure of pentacene-doped naphthalene, where a , b , and c denote the crystallographic axes. The cleaved surface corresponds to the ab -plane. (b) Pentacene molecules substitute into two inequivalent lattice sites of the naphthalene host, giving rise to two crystallographically distinct molecular orientations. Both orientations share a common molecular long axis (defined as the X -axis), which lies in the ac -plane and is tilted by approximately 10° from the c -axis. The local molecular frames are denoted XOY_1 and XOY_2 , where Y_1 and Y_2 lie along the short molecular axis within the molecular plane. The Hamiltonian in Eq. (1) is expressed in this molecular frame. The Y_1 - and Y_2 - axes are symmetrically split about the ac -plane by 47° . For convenience, we define an orthonormal sensing frame $XY'Z'$, where X coincides with the molecular long axis, Z' is aligned with the crystal b -axis, and Y' bisects the angle between y_1 and y_2 . (c) Schematic of the experimental setup showing the crystal cleavage plane (ab -plane). The a - and b -axes can be identified independently [32]. Microwave excitation is delivered using a coplanar-waveguide stripline, and optical excitation (532 nm, 0.1 mW) and readout are performed with a confocal microscope. (d) Energy-level diagram of pentacene and relevant inter-level transitions. Green and orange arrows denote optical excitation and fluorescence, respectively, while gray arrows represent the non-radiative intersystem crossing (ISC) processes. The ISC coupling to the T_X sublevel is stronger than to T_Y or T_Z . Microwave fields can drive transitions between the triplet spin-states. (e) Optically detected magnetic resonance (ODMR) spectra of the $T_X \leftrightarrow T_Z$ and $T_Y \leftrightarrow T_Z$ transitions measured at zero magnetic field. The linewidths are obtained from Lorentzian fitting.

II. ROOM-TEMPERATURE VECTOR AC SENSING

A. Pentacene sample and spin properties

We used high-quality pentacene-doped naphthalene single crystals with a pentacene concentration of about 4×10^{-5} mol/mol [32] (see supplementary materials [33] for detailed sample preparation and characterization). In pentacene doped into naphthalene crystals, the pentacene molecules align along two crystallographically distinct orientations from substitution of the naphthalene

host at inequivalent lattice sites, as shown in Fig. 1(a). These orientations are fixed relative to the crystal axes, thereby establishing a well-defined geometric relation between the molecular frames and the laboratory sensing frame [Fig. 1(b)].

The naphthalene lattice vectors \vec{a} and \vec{b} define the cleavage (ab) plane, which can be experimentally identified through birefringence or angle-resolved optical measurements [32]. In our confocal microscope setup, the laboratory sensing frame is aligned with respect to this crystallographic axis system, as illustrated in Fig. 1(c).

At zero external magnetic field, the two molecular orientations of pentacene are energetically degenerate. The

simplified energy-level structure of an individual pentacene molecule in Fig. 1(d) [19, 20] highlights the presence of a spin-triplet metastable state. Under optical excitation, population can be pumped from the singlet ground state (S_0) to the excited singlet state (S_1), from which it can either decay radiatively back to S_0 or undergo spin-dependent intersystem crossing (ISC) into the triplet manifold (T_X , T_Y , T_Z). The spin-dependent ISC process preferentially populates the T_X state, enabling optical spin polarization [34]. To prepare an initial triplet polarized on other sublevels, a fast (~ 100 ns) flip microwave pulse is employed immediately after laser pumping.

Because the decay rates Γ_μ ($\mu = X, Y, Z$) from the triplet sublevels to the ground state S_0 are unequal, the population of the S_0 state after a delay time t_d encodes information about the previous excited spin state. The resulting photoluminescence (PL), which is proportional to the population in S_0 , thus provides spin-dependent contrast and enables optical readout of the triplet manifold.

We define the orthogonal molecular frame such that the X - and Y -axes align with the long and short molecular axes of an individual pentacene molecule, respectively (frames XOY_1 and XOY_2 in Fig. 1(b), noting that the two orientations share the same X -axis). In this molecular frame, the triplet energy levels are described by the Hamiltonian

$$\mathcal{H} = DS_Z^2 - E(S_X^2 - S_Y^2), \quad (1)$$

with zero-field splitting parameters $D = 1389$ (2π)MHz and $E = -48$ (2π)MHz, which need to be experimentally determined for each host matrix. Transitions between the triplet eigenstates can be driven by a microwave field $\vec{B}_{ac}(t) \cdot \vec{S}$ through the nonzero matrix elements

$$\langle T_X | S_Z | T_Y \rangle = \langle T_Z | S_Y | T_X \rangle = \langle T_Y | S_X | T_Z \rangle = 1. \quad (2)$$

Therefore, any pair of triplet sublevels can serve as a qubit. To correct for imperfect state preparation and optical collection, we normalize the raw PL signal by a reference PL measured at the same delay t_d after initializing the system (e.g. $|T_\mu\rangle$). Assuming we operate in a qubit manifold with populations $|\alpha|^2 + |\beta|^2 = 1$ for the two states μ, ν , the normalized signal is thus

$$\text{Sig} = 1 - |\beta|^2 \frac{e^{-(\Gamma_\nu t_d)^{\iota_\nu}} - e^{-(\Gamma_\mu t_d)^{\iota_\mu}}}{1 - e^{-(\Gamma_\mu t_d)^{\iota_\mu}}} = 1 - |\beta|^2 C(t_d), \quad (3)$$

where the stretch exponents $\iota_{\mu,\nu}$ capture the multichannel relaxation pathways. This defines the readout contrast $C(t_d)$. Experimentally, $t_d = 30$ μ s and 47 μ s maximize the contrast for the $T_X \leftrightarrow T_Z$ and $T_Y \leftrightarrow T_Z$ qubits, respectively.

Figure 1(e) shows the optically detected magnetic resonance (ODMR) of the $T_X \leftrightarrow T_Z$ ($\omega_{xz} = D - E$) and $T_Y \leftrightarrow T_Z$ ($\omega_{yz} = D + E$) transitions at zero magnetic field.

B. Principle and experimental demonstration

According to Eq. (2), since each transition between pairs of triplet states couples to a specific component of the microwave magnetic field, the corresponding Rabi frequency encodes directional information of an external AC field. Thus, it would be possible to perform vector AC magnetometry at the level of a single pentacene molecule.

A more compact protocol can be obtained exploiting the different pentacene orientations in the crystal, similar to prior schemes with NVs [35, 36]. As discussed above, the two pentacene orientations share a common molecular X -axis but have distinct Y -axes (Y_1 and Y_2). Therefore, when an AC microwave field is applied, the $T_Y \leftrightarrow T_Z$ transition in both orientations is driven equally by the X -component of the field, whereas the $T_X \leftrightarrow T_Z$ transition probes the orientation-dependent y -components (Y_1 and Y_2), as illustrated in the inset of Fig. 2(d), similarly to prior schemes with NVs [36, 37]. Consequently, Rabi measurement of $T_X \leftrightarrow T_Z$ transitions yields two Rabi frequencies (Ω_{Y_1} , Ω_{Y_2}) from the two orientations [Fig. 2(b,d)] and one (Ω_X) from the $T_Y \leftrightarrow T_Z$ transition [Fig. 2(c,d)]. This three-axis projection scheme enables full reconstruction of the three-dimensional AC magnetic-field vector. For simplicity, we define the orthogonal laboratory sensing frame $XY'Z'$, where the Y' axis bisects the molecular Y_1 and Y_2 axes [Fig. 1(b) and Fig. 2(d), inset] and Z' -axis aligns with the b axis of naphthalene lattice. The AC magnetic-field components in this frame can be reconstructed as

$$\begin{aligned} \gamma_e B_X &= \Omega_X, \\ \gamma_e B_{Y'} &= \frac{\Omega_{Y_1} + \Omega_{Y_2}}{2 \cos \phi}, \\ \gamma_e B_{Z'} &= \frac{\Omega_{Y_1} - \Omega_{Y_2}}{2 \sin \phi}, \end{aligned} \quad (4)$$

where γ_e is the electron spin gyromagnetic ratio of pentacene, equal to that of a free electron.

The Rabi oscillation appears as a damped oscillation signal with a characteristic decay time $T_{2\rho}$. Considering both photon shot noise and the finite spin coherence time, the sensitivity η of the Rabi protocol is given by [38, 39]

$$\eta = \frac{\sigma_S}{C(t_d)} \frac{e^{t/T_{2\rho}}}{\gamma_e t} \sqrt{T}, \quad (5)$$

where t is the interrogation time and $C(t_d)$ the optical contrast from equation 3, with waiting time t_d . $T = 500$ μ s denotes the total experimental cycle time, which includes the sequence duration and a post-delay time T_d that resets the population before each repetition of the sequence. [Fig. 2 (a)]. σ_S represents the relative standard deviation of the normalized signal and is typically governed by photon shot noise. The optimal interrogation time is set by the Rabi decay time, $t \approx T_{2\rho} \approx 3$ μ s for an AC magnetic field with amplitude

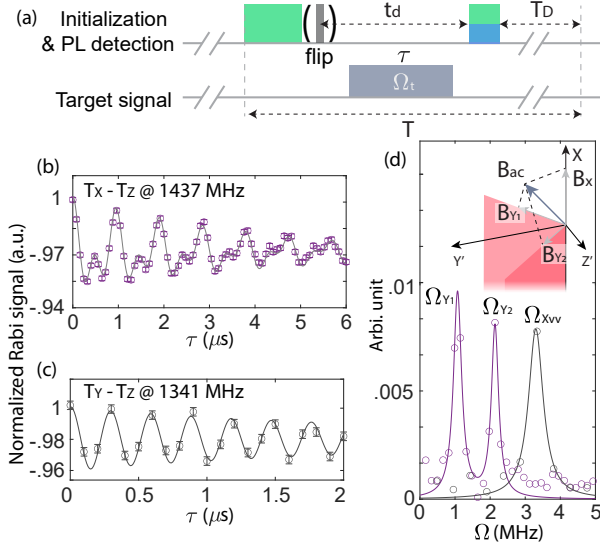


FIG. 2. **Vector AC sensing using two pentacene orientations.** (a) Experimental pulse sequence for ODMR and Rabi sensing. The green and blue blocks denote optical initialization and photon collection, respectively. An optional, short (~ 100 ns) flip pulse maps the initial T_X state to T_Y when we target the $T_Y \leftrightarrow T_Z$ transition. After applying the continuous target driving Ω_t , optical readout is performed following a delay time t_d , during which the triplet sublevels relax at different rates, generating fluorescence contrast between spin states. A post-detection delay time T_D is needed after each PL measurement to reset the population, yielding the total sequence time $T \approx 500 \mu$ s. (b–d) Optically detected Rabi oscillations of the $T_X \leftrightarrow T_Z$ (b) and $T_Y \leftrightarrow T_Z$ (c) transitions, and their corresponding Fourier spectra (d). Purple and gray curves show the $T_X \leftrightarrow T_Z$ and $T_Y \leftrightarrow T_Z$ transitions, respectively. The Rabi frequencies are proportional to the projection of the applied AC magnetic field onto the relevant molecular axis (inset), e.g., $\Omega_{Y1} = \gamma_e B_{Y1}$. Error bars reflect photon shot noise and are obtained by propagating the standard deviation of the measured photon counts through signal normalization.

$|B_{ac}/\gamma_e| \sim 0.5$ (2π) MHz. This corresponds to a sensitivity of $\eta \approx 3.6 \mu\text{T}/\sqrt{\text{Hz}}$ for all three molecular axes. Notably, in the relevant regime where $T_{2\rho} \ll T$, the optical readout sensitivity scales as $\eta \propto 1/T_{2\rho}$.

While we demonstrated the feasibility of optically detected molecular-spin-based vector magnetometry, the performance, especially the sensitivity of the simple Rabi protocol, remains substantially below that of other solid-state spin sensors. In the following, we analyze the sources of noise that limit the coherence time in order to devise a control strategy to improve the sensor performance.

III. ROBUST MODULATED AC SENSING

A. Decoherence sources in driven pentacene spin systems

The dominant sources of decoherence arise from the nuclear spin bath, from slowly varying spatial inhomogeneities of the static field, and from variations in the microwave amplitude due to electronic noise or spatial inhomogeneity of the drive. We can thus model the noise as a stochastic magnetic field that is added to the driving Hamiltonian,

$$H(t) = \Omega_1[1 + \xi_{\Omega_1}(t)] \cos(\omega_0 t) \sigma_X + \xi_Z \sigma_Z + \xi_X \sigma_X, \quad (6)$$

where ξ_j denotes a stochastic magnetic field with power spectral density (PSD) $S_j(\nu) = \int_{-\infty}^{\infty} dt e^{i\nu t} \langle \xi_j(t) \xi_j(0) \rangle$, $j \in \{z, x, \Omega_1\}$. Here $\xi_Z(t)$ and $\xi_X(t)$ are longitudinal and transverse stochastic magnetic fields, respectively, and $\xi_{\Omega_1}(t)$ represents relative fluctuations in the drive amplitude.

When the goal is to sense weak AC fields, ξ_{Ω_1} can be neglected and longitudinal inhomogeneous broadening limits the coherence time. In deuterated pentacene, the observed ~ 0.6 (2π) MHz linewidth is dominated by hyperfine coupling to the deuterons in the pentacene molecule [19, 40]. This coupling introduces a distribution of quasi-static detunings $\delta\omega$ that yield an effective Rabi frequency $\Omega_R(\delta\omega) = \sqrt{\Omega_1^2 + \delta\omega^2}$. At low microwave amplitudes ($\Omega_1 \lesssim \delta\omega$), the finite linewidth introduces a bias in the Rabi oscillation frequency, faster dephasing, and reduces the contrast [33], thereby degrading the sensing accuracy [41, 42]. A simple strategy to mitigate the broadening effects would be to add a bias driving field to the target AC, in order to operate at larger driving strengths. When $\langle \Omega_R \rangle \approx \Omega_1 + \langle \delta\omega^2 \rangle / 2\Omega_1$, detuning-induced decoherence and bias is strongly suppressed.

In this strong-driving limit, relaxation can be quantified by the generalized Bloch-equation (GBE) framework [43, 44]. Moving to the rotating frame at resonant frequency ω_0 , the longitudinal and transverse (Rabi) relaxation rates are given by

$$\begin{aligned} \frac{1}{T_{1\rho}} &= S_Z(\Omega_1) + \frac{1}{2} S_X(\omega_0), \\ \frac{1}{T_{2\rho}} &= \frac{1}{2T_{1\rho}} + \frac{1}{2} S_X(\omega_0) + \frac{1}{4} S_{\Omega_1}(0). \end{aligned} \quad (7)$$

The relaxation time $T_{1\rho}$ depends marginally on the transverse noise, as it is only affected by spectral density components, $S_X(\omega_0)$, around the high frequency ω_0 . Thus, the longitudinal relaxation is governed by $S_Z(\Omega)$, longitudinal noise spectral components at frequency around the dressed-state splitting Ω_1 . We determine $S_Z(\nu)$ by measuring $T_{1\rho}$ with a spin-locking experiment [45, 46] see insets of Fig. 3 (a). The results show that the spectrum is zero-frequency centered, consistent with slow fluctuations from the nuclear-spin envi-

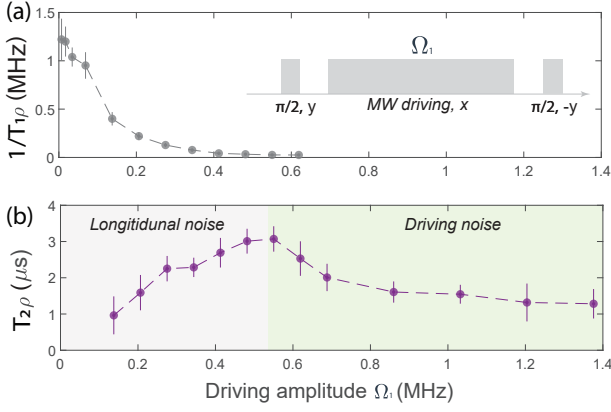


FIG. 3. Pentacene coherence under continuous driving. (a) Microwave pulse sequence for spin locking and measured longitudinal relaxation times $T_{1\rho}$ at varying driving amplitudes. Each point results from fitting an exponential decay on the spin-locking signal for varying MW driving duration. The decay rate $1/T_{1\rho}$ reflects the longitudinal noise spectrum $S_Z(\nu)$ evaluated at the driving strength. (b) Rabi relaxation time $T_{2\rho}$ (sequence in Fig. 2.a) as a function of the driving amplitude. The decrease in $T_{2\rho}$ at weak drive arises from magnetic-field fluctuations and hyperfine-induced spectral broadening, while the reduction at strong drive is dominated by microwave-amplitude noise. Error bars represent the 95% confidence intervals of the damped Rabi oscillation fit.

ronment. Combined with the hyperfine-induced inhomogeneous broadening analyzed above, this explains both the rapid decoherence at weak drive and its suppression as the drive amplitude increases. However, as we increase the driving amplitude Ω_1 the effects of its inhomogeneity and fluctuation on the Rabi coherence increases, see Fig. 3 (b), since $S_{\Omega_1} \propto \Omega_1$ [44]. For slow varying amplitude fluctuations (with correlation time \gg interrogation time), the decoherence exhibits a Gaussian decay envelope with a rate proportional to Ω_1 (detailed derivation in the supplementary materials [33].)

Taken together, our experimental results and noise model reveal a fundamental limitation to the bandwidth and sensitivity of Rabi-based sensing. At low drive amplitudes, the sensing performance degrades due to inhomogeneous detuning broadening and quasi-static magnetic noise. At high drive amplitudes, the coherence becomes limited by microwave inhomogeneity, consistent with the observed variation of $T_{2\rho}$ across different driving conditions.

B. Phase alternation for enhanced Rabi sensing

To extend the driven-state coherence and enable robust Rabi-type sensing, we adopt a rotary-echo (RE) scheme [29] to protect the coherence of the continuous target field drive. The protocol applies a strong resonant drive whose phase is periodically inverted at intervals

τ [Fig. 4(a)], thus canceling drive imperfections. Similar coherence protection is achieved with more complex piece-wise constant [47–50] or continuous phase modulation, such as by concatenated continuous dynamical decoupling (CCDD) [44, 51]. Such techniques have also been applied to coherent sensing in the radio-frequency band [30, 31, 52, 53]. Recently, CCDD-based protocols [42, 54, 55] and frequency mixing [53] were proposed to improve microwave sensing, but their performance was still limited by a reduction of the target field amplitude or by drive-induced inhomogeneities. Here, we show that our rotary-echo approach effectively refocus drive-induced errors while preserving the desired decoupling from external magnetic fields.

In our scheme, we implement a periodic train of rotary echoes with alternating phases, where the protecting drive is always oriented with the target field, ensuring that the evolution generated by the control is properly time-reversed. After an even number of inversions, the qubit recovers a clean Rabi oscillation governed solely by the transverse target field. The resulting Rabi frequencies can then be directly used for the microwave-field vector reconstruction discussed in the previous section.

Experimentally, we observe a substantial extension of the driven-state coherence time under the RE control. As shown in Fig. 4(b), under a weak target field ($\Omega_t \sim 0.2$ (2π)MHz) between the $T_X \leftrightarrow T_Z$ transition, the simple Rabi protocol produces barely visible oscillations, whereas the RE sequence with strong driving ($\Omega_c = 2.625$ (2π)MHz, $\tau = 390$ ns) restores clear, long-lived coherence. The coherence time as a function of the target-field amplitude is shown in Fig. 4(c), demonstrating that RE extends the driven-state coherence by nearly an order of magnitude compared to the standard Rabi protocol.

A similar improvement is also observed for the $T_Y \leftrightarrow T_Z$ transition when the RE control is applied ([33]). The same vector-field reconstruction procedure described in Eq. (4) can be implemented under the RE control. The sensitivity for the vector field with extended $T_{2\rho}$ is $(\eta_X, \eta_{Y'}, \eta_{Z'}) = (0.8, 0.5, 1.1) \mu T/\sqrt{\text{Hz}}$, comparable to solid-state spin sensors operated under finite static magnetic fields [35].

C. Coherence protection mechanisms

To elucidate the protection offered by the RE scheme and identify optimal driving parameters, we analyze the driven-spin dynamics still using the GBE framework.

The Hamiltonian in Eq. (6) is modified by substituting the term proportional to Ω_1 with

$$H_{\mu w} = \frac{1}{2} [\Omega_t + \Omega_c s(t)(1 + \xi_{\Omega_c}(t))] \sigma_X, \quad (8)$$

where we neglected noise from the target field. Here $\xi_{\Omega_c}(t)$ denote relative fluctuations of the control ampli-

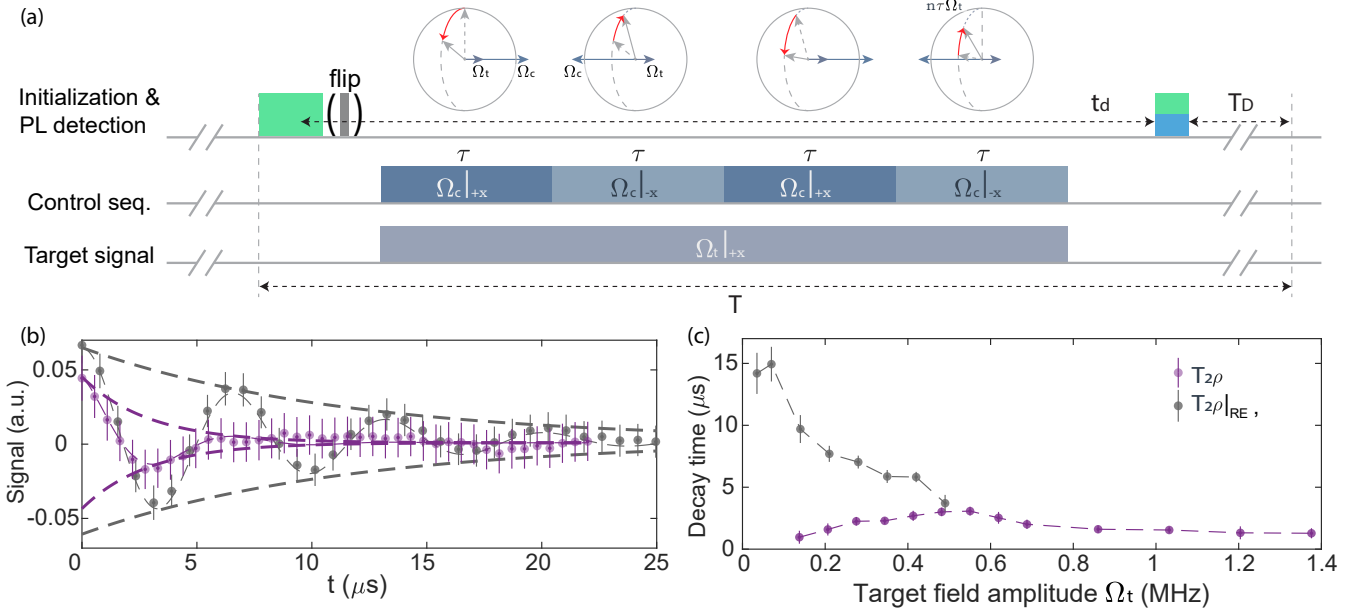


FIG. 4. **Rotary-echo sensing protocol.** (a) Experimental sequence for sensing. The RE control sequence consists strong microwave driving of amplitude Ω_c with π phase flips after each multiple of τ . The target signal to be sensed is continuously applied Ω_t . The flip pulse is still for $T_Y \leftrightarrow T_Z$ transition only. (b) Rabi oscillations without (purple) and with (gray) the control sequence on the $T_X \leftrightarrow T_Z$ transition performed at a target Rabi frequency of 0.17 (2π)MHz. Here the normalized signals are centered around zero for clear comparison of the coherence and contrast between the two scenarios. (c) Decay time, $T_{2\rho}$, versus target field amplitude, Ω_t , in the case of no-control and RE (with $\Omega_c = 2.625$ (2π)MHz, $\tau = 390$ ns). Note that in the case of weak driving, the RE control vastly lengthens the coherence time—about an order of magnitude longer than the simple Rabi driving.

tudes, and $s(t) = \pm 1$ implements the periodic inversions with period 2τ .

The RE control modifies the dressed-state dynamics in two key ways. First, dephasing arising from amplitude fluctuations of the control field are modulated by the periodic inversion function $s(t)$ and efficiently suppressed. The modulation generates a filter function that modifies the response to the noise spectrum $S_{\Omega_c}(\nu)$ from zero frequency to the odd harmonics of the modulation frequency π/τ [56, 57]. The resulting dephasing rate contributed by the control-field amplitude noise is centered around these higher harmonics,

$$\Gamma_{\Omega_c} \approx \sum_{m=-\infty}^{\infty} \frac{1}{(2m+1)^2} S_{\Omega_c} \left[\frac{(2m+1)\pi}{\tau} \right], \quad (9)$$

and thus effectively suppressed.

Second, the phase modulation modifies the longitudinal-noise decoupling and care should be taken to ensure that it is still effective. Indeed, the periodic phase inversions generate Floquet sidebands in the dressed-state splitting [30, 31, 58], modifying the frequency components of the noise that satisfy the dressed-state resonance condition. In the strong-control limit ($\Omega_c \gg \Omega_t$), the longitudinal relaxation due to the

ξ_Z is:

$$\frac{1}{T_{1\rho}} \Big|_{\text{R-SE}} \approx \sum_{m=-\infty}^{\infty} \frac{1}{(2m+1)^2} S_Z \left[\Omega_c - \frac{(2m+1)\pi}{\tau} \right]. \quad (10)$$

By choosing sufficiently large Ω_c and appropriate inversion spacing τ , the dominant Floquet sideband frequencies are shifted far from zero. Experimentally [Fig. 4(b,c)], we set $\Omega_c \tau = 2\pi$, which places the dominant coupling near $\Omega_c/2$, well separated from the zero-frequency peak of $S_Z(\nu)$. This effectively decouples the dressed states from low-frequency bath fluctuations.

The RE protocol provides an effective biasing scheme to enhance Rabi-based sensing, enabling accurate weak-field detection and enhancing the vector sensitivities demonstrated in this work.

IV. DISCUSSION AND OUTLOOK

In this work, we propose and experimentally demonstrate a protocol that employs photoexcited pentacene triplet spins in a naphthalene crystal as a vector AC magnetometer operating at room temperature and zero static field. The three-dimensional components of an AC magnetic field are reconstructed from the Rabi frequencies of selected transitions from the two crystallographic

pentacene orientations in naphthalene crystal. The insights gained by experimentally evaluating and theoretically modeling the noise affecting the sensor lead us to introduce the rotary-echo quantum sensing protocol, which significantly improves sensitivity by protecting the spin coherence. The proof-of-concept implementation in this work achieves sensitivities comparable to established solid-state defect sensors, on the order of $\sim 1 \mu\text{T}/\sqrt{\text{Hz}}$.

Experimental evidence indicates an inherent bandwidth-sensitivity trade-off for standard Rabi sensing. The longitudinal noise limits the sensitivity in low field regime, while the inhomogeneity of the strong drive introduces additional dephasing. The rotary echo sequence applies strong driving with periodic phase inversions which refocuses the inhomogeneous drive amplitudes. This provides a perfect biasing of the weak field to the strong driving regime, thus effectively decouples to the noise field. The resulting lifetime of the dressed-state coherence is significantly extended in an order of magnitude, enabling accurate, broadband estimation of weak AC fields. The coherence enhancement provided by RE is particularly important for pentacene-based protocols, which necessitates a substantial overhead time to build spin-state contrast, causing the overall sensitivity to scale linearly with the available coherence.

For general photoexcited molecular spin systems, this long overhead time is often a disadvantage with respect to ground-state solid-state defect sensors. However, as we demonstrate, molecular ensembles can achieve comparable sensitivities, benefiting from their significantly higher spin densities while still preserving long coherence times. Practically, the sensitivity can be further amplified. Throughout our experiments, only $\sim 60\%$ of the spins in the detection volume were optically polarized [33] and even less are detected. This initialization efficiency can have $1.25\times$ increase when using a 552 nm pump laser, corresponding to the room temperature absorption maximum of pentacene [32].

An important advantage of using pentacene molecular spins to perform AC magnetometry is the possibility to work at zero external magnetic field, as we demonstrated. In this regime, the accuracy and sensitivity of traditional solid-state defect sensors degrade due to local strain, charge and external defects that induce state mixing and decoherence [16, 59–62]. Additionally, the triplet level structure of pentacene is intrinsically tolerant to small background magnetic fields, whose influence is quadratically suppressed, (e.g., producing less than $20 (2\pi)$ kHz

resonance shifts and negligible state mixing under Earth magnetic field). This insensitivity to weak fields makes pentacene a robust and practically convenient platform in unshielded or imperfectly controlled environments.

To achieve better performance in quantum sensing, molecular spin systems offer unique opportunities for chemical engineering, including nuclear-spin [63, 64] or ligand modification [65–67], as well as programmable spatial placement of the spin hosts [46, 68]. The former allows tailoring the spin properties; for example, further deuteration of the naphthalene host can suppress nuclear-spin noise and extend coherence [46, 69, 70]. The latter enables precise positioning of molecular spins, for instance through metal-organic framework architectures [71–73], opening pathways toward controllable non-local correlation sensing.

These advantages have long motivated interest in exploring molecular spin-qubit platforms, pursuing better coherence properties, enhanced robustness and more environmentally suitable form factors. Our work bridges these principles into practice, establishing a powerful and scalable approach for room-temperature quantum sensing.

V. ACKNOWLEDGMENT

We thank Ashok Ajoy, Shimon Kolkowitz, Andrew Stasiuk, Bo Xing, Keyuan Zhong for helpful discussions. This work was supported in part by the National Science Foundation under Grants No. PHY2317134 (Center for Ultracold Atoms). B. L. thanks MathWorks for their support in the form of a Graduate Student Fellowship. The opinions and views expressed in this publication are from the authors and not necessarily from MathWorks.

VI. AUTHOR CONTRIBUTIONS

B.L., Y.Q., G.H., and P.C. conceived the idea. B.L. and G.H. implemented experiments with assistance from A.U and J.Y., and analyzed the data. Y.Q. and P.H. were responsible for pentacene-naphthalene synthesis. P.C. supervised the project. All authors discussed the results.

CONFLICTS OF INTEREST

The authors declare no conflict of interest.

-
- [1] J. M. Taylor, P. Cappellaro, L. Childress, L. Jiang, D. Budker, P. R. Hemmer, A. Yacoby, R. Walsworth, and M. D. Lukin, *Nature Physics* **4**, 810 (2008).
 - [2] J. R. Maze, P. L. Stanwix, J. S. Hodges, S. Hong, J. M. Taylor, P. Cappellaro, L. Jiang, M. V. G. Dutt, E. Togan,

- A. S. Zibrov, A. Yacoby, R. L. Walsworth, and M. D. Lukin, *Nature* **455**, 644 (2008).
- [3] L. M. Pham, D. Le Sage, P. L. Stanwix, T. K. Yeung, D. Glenn, A. Trifonov, P. Cappellaro, P. R. Hemmer, M. D. Lukin, H. Park, A. Yacoby, and R. L. Walsworth,

- New Journal of Physics **13**, 045021 (2011).
- [4] P. Neumann, I. Jakobi, F. Dolde, C. Burk, R. Reuter, G. Waldherr, J. Honert, T. Wolf, A. Brunner, J. H. Shim, D. Suter, H. Sumiya, J. Isoya, and J. Wrachtrup, *Nano Letters* **13**, 2738 (2013).
 - [5] G. Wang, A. R. Barr, H. Tang, M. Chen, C. Li, H. Xu, A. Stasiuk, J. Li, and P. Cappellaro, *Physical Review Letters* **131**, 043602 (2023).
 - [6] E. Lee-Wong, R. Xue, F. Ye, A. Kreisel, T. van Der Sar, A. Yacoby, and C. R. Du, *Nano Letters* **20**, 3284 (2020).
 - [7] T. Van der Sar, F. Casola, R. Walsworth, and A. Yacoby, *Nature communications* **6**, 7886 (2015).
 - [8] S. E. Lillie, N. Dontschuk, D. A. Broadway, D. L. Creedon, L. C. Hollenberg, and J.-P. Tetienne, *Physical Review Applied* **12**, 024018 (2019).
 - [9] A. Nowodzinski, M. Chipaux, L. Toraille, V. Jacques, J.-F. Roch, and T. Debuisschert, *Microelectronics Reliability* **55**, 1549 (2015).
 - [10] Y. Tan, X. Hu, Y. Hou, and Z. Chu, *Membranes* **12**, 957 (2022).
 - [11] B. S. Miller, L. Bezinge, H. D. Gliddon, D. Huang, G. Dold, E. R. Gray, J. Heaney, P. J. Dobson, E. Nastoouli, J. J. Morton, *et al.*, *Nature* **587**, 588 (2020).
 - [12] H. Zhou, J. Choi, S. Choi, R. Landig, A. M. Douglas, J. Isoya, F. Jelezko, S. Onoda, H. Sumiya, P. Cappellaro, H. S. Knowles, H. Park, and M. D. Lukin, *Physical Review X* **10**, 031003 (2020).
 - [13] R. Ghassemizadeh, W. Körner, D. F. Urban, and C. Elsässer, *Physical Review B* **110**, 205148 (2024).
 - [14] E. Bauch, S. Singh, J. Lee, C. A. Hart, J. M. Schloss, M. J. Turner, J. F. Barry, L. M. Pham, N. Bar-Gill, S. F. Yelin, *et al.*, *Physical Review B* **102**, 134210 (2020).
 - [15] H. Park, J. Lee, S. Han, S. Oh, and H. Seo, *npj Quantum Information* **8**, 95 (2022).
 - [16] T. Mittiga, S. Hsieh, C. Zu, B. Kobrin, F. Machado, P. Bhattacharyya, N. Z. Rui, A. Jarmola, S. Choi, D. Budker, and N. Y. Yao, *Physical Review Letters* **121**, 246402 (2018).
 - [17] J. Köhler, J. A. J. M. Disselhorst, M. C. J. M. Donckers, E. J. J. Groenen, J. Schmidt, and W. E. Moerner, *Nature* **363**, 242 (1993).
 - [18] J. Wrachtrup, C. von Borczyskowski, J. Bernard, M. Orrit, and R. Brown, *Nature* **363**, 244 (1993).
 - [19] H. Singh, N. D'Souza, K. Zhong, E. Druga, J. Oshiro, B. Blankenship, R. Montis, J. A. Reimer, J. D. Breeze, A. Ajoy, *et al.*, *Physical Review Research* **7**, 013192 (2025).
 - [20] A. Mena, S. K. Mann, A. Cowley-Semple, E. Bryan, S. Heutz, D. R. McCamey, M. Attwood, and S. L. Bayliss, *Physical Review Letters* **133**, 120801 (2024).
 - [21] H. Singh, N. D'Souza, J. Garrett, A. Singh, B. Blankenship, E. Druga, R. Montis, L. Z. Tan, and A. Ajoy, *Nature Communications* **16**, 10530 (2025).
 - [22] A. Yamauchi, S. Fujiwara, N. Kimizuka, M. Asada, M. Fujiwara, T. Nakamura, J. Pirillo, Y. Hijikata, and N. Yanai, *Nature communications* **15**, 7622 (2024).
 - [23] J. M. Zadrozny, A. T. Gallagher, T. D. Harris, and D. E. Freedman, *Journal of the American Chemical Society* **139**, 7089 (2017).
 - [24] S. L. Bayliss, D. W. Laorenza, P. J. Mintun, B. D. Kovos, D. E. Freedman, and D. D. Awschalom, *Science* **370**, 1309 (2020).
 - [25] K. Pei, *Surfaces and Interfaces* **30**, 101887 (2022).
 - [26] F. Moro, M. Moret, A. Ghirri, A. Granados del Águila, Y. Kubozono, L. Beverina, and A. Cassinese, *Journal of Materials Research* **37**, 1269–1279 (2022).
 - [27] Y.-Y. Lin, D. J. Gundlach, S. F. Nelson, and T. N. Jackson, *IEEE Transactions on Electron Devices* **44**, 1325 (1997).
 - [28] Y. Yunus, N. A. Mahadzir, M. N. Mohamed Ansari, T. H. Tg Abd Aziz, A. Mohd Afdzaluddin, H. Anwar, M. Wang, and A. G. Ismail, *Polymers* **14**, 1112 (2022).
 - [29] I. Solomon, *Physical Review Letters* **2**, 301 (1959).
 - [30] C. D. Aiello, M. Hirose, and P. Cappellaro, *Nature Communications* **4**, 1419 (2013).
 - [31] M. Hirose, C. D. Aiello, and P. Cappellaro, *Physical Review A—Atomic, Molecular, and Optical Physics* **86**, 062320 (2012).
 - [32] Y. Quan, N. Niketic, J. M. Steiner, T. R. Eichhorn, W. Tom Wenckebach, and P. Haultle, *Molecular Physics* **121** (2023), 10.1080/00268976.2023.2169025.
 - [33] Supplemental Materials: Robust AC vector sensing at zero magnetic field with pentacene.
 - [34] H. Wu, W. Ng, S. Mirkhanov, A. Amirzhan, S. Nitnara, and M. Oxborrow, *Journal of Physical Chemistry C* **123**, 24275 (2019).
 - [35] P. Wang, Z. Yuan, P. Huang, X. Rong, M. Wang, X. Xu, C. Duan, C. Ju, F. Shi, and J. Du, *Nature communications* **6**, 6631 (2015).
 - [36] J. M. Schloss, J. F. Barry, M. J. Turner, and R. L. Walsworth, *Physical Review Applied* **10**, 034044 (2018).
 - [37] H. Clevenston, L. M. Pham, C. Teale, K. Johnson, D. Englund, and D. Braje, *Applied Physics Letters* **112**, 252406 (2018).
 - [38] C. L. Degen, F. Reinhard, and P. Cappellaro, *Reviews of modern physics* **89**, 035002 (2017).
 - [39] J. F. Barry, J. M. Schloss, E. Bauch, M. J. Turner, C. A. Hart, L. M. Pham, and R. L. Walsworth, *Reviews of Modern Physics* **92**, 015004 (2020).
 - [40] Y. Quan, *Development of Triplet Dynamic Nuclear Polarization for Polarization Analysis in Small-Angle Neutron Scattering*, Ph.d. thesis, University of Basel, Basel, Switzerland (2021), original document archived on the document server of the University of Basel (edoc.unibas.ch).
 - [41] E. Billaud, L. Balembois, J. Travesedo, M. Le Dantec, M. Rančić, E. Albertinale, R. Truong, S. Bertaina, T. Chanélière, P. Goldner, *et al.*, *Physical Review Research* **7**, 013011 (2025).
 - [42] T. Kitamura, G. Genov, A. Salhov, Y. Kobayashi, S. Onoda, J. Isoya, A. Retzker, and F. Jelezko, *arXiv preprint* (2025).
 - [43] E. Geva, R. Kosloff, and J. Skinner, *The Journal of chemical physics* **102**, 8541 (1995).
 - [44] G. Wang, C. Munuera-Javaloy, Y.-X. Liu, Y. Zhu, J. del Pino, and P. Cappellaro, *New Journal of Physics* **22**, 123045 (2020).
 - [45] A. Abragam, *The Principles of Nuclear Magnetism*, International Series of Monographs on Physics (Oxford University Press, Oxford, 1961).
 - [46] B. Li, Y. Quan, X. Li, G. Wang, R. G. Griffin, A. R. Harutyunyan, and P. Cappellaro, *arXiv preprint arXiv:2511.03199* (2025).
 - [47] M. H. Levitt and R. Freeman, *Journal of Magnetic Resonance* (1969) **43**, 502 (1981).
 - [48] M. H. Levitt, R. Freeman, and T. Frenkiel, *Journal of Magnetic Resonance* **47**, 328 (1982).

- [49] A. J. Shaka, J. Keeler, and R. Freeman, *Journal of Magnetic Resonance* **53**, 313 (1983).
- [50] A. J. Shaka, C.-J. Lee, and A. Pines, *Journal of Magnetic Resonance* **77**, 274 (1988).
- [51] J.-M. Cai, B. Naydenov, R. Pfeiffer, L. P. McGuinness, K. D. Jahnke, F. Jelezko, M. B. Plenio, and A. Retzker, *New Journal of Physics* **14**, 113023 (2012).
- [52] G. Wang, Y.-X. Liu, Y. Zhu, and P. Cappellaro, *Nano Letters* **21**, 5143–5150 (2021).
- [53] G. Wang, Y.-X. Liu, J. M. Schloss, S. T. Alsid, D. A. Braje, and P. Cappellaro, *Physical Review X* **12**, 021061 (2022).
- [54] A. Stark, N. Aharon, T. Unden, D. Louzon, A. Huck, A. Retzker, U. L. Andersen, and F. Jelezko, *Nature Communications* **8**, 1105 (2017).
- [55] A. Salhov, Q. Cao, J. Cai, A. Retzker, F. Jelezko, and G. Genov, *Phys. Rev. Lett.* **132**, 223601 (2024).
- [56] G. A. Álvarez and D. Suter, *Physical review letters* **107**, 230501 (2011).
- [57] J. Bylander, S. Gustavsson, F. Yan, F. Yoshihara, K. Harrabi, G. Fitch, D. G. Cory, Y. Nakamura, J.-S. Tsai, and W. D. Oliver, *Nature Physics* **7**, 565 (2011).
- [58] K. L. Ivanov, K. R. Mote, M. Ernst, A. Equbal, and P. K. Madhu, *Progress in Nuclear Magnetic Resonance Spectroscopy* **126**, 17 (2021).
- [59] P. J. Vetter, A. Marshall, G. T. Genov, T. F. Weiss, N. Striegler, E. F. Großmann, S. Oviedo-Casado, J. Cerrillo, J. Prior, P. Neumann, and F. Jelezko, *Physical Review Applied* **17**, 044028 (2022).
- [60] H. Zheng, J. Xu, G. Z. Iwata, T. Lenz, J. Michl, B. Yavkin, K. Nakamura, H. Sumiya, T. Ohshima, J. Isoya, J. Wrachtrup, A. Wickenbrock, and D. Budker, *Physical Review Applied* **11**, 064068 (2019).
- [61] P. Udvarhelyi, V. O. Shkolnikov, A. Gali, G. Burkard, and A. Pályi, *Physical Review B* **98**, 075201 (2018).
- [62] A. Ungar, H. Tang, A. Stasiuk, B. Xing, B. Li, J. Li, A. Cooper, and P. Cappellaro, *arXiv preprint* (2025).
- [63] D. Atzrodt, V. Derdau, W. J. Kerr, and M. Reid, *Angewandte Chemie International Edition* **57**, 1758 (2018).
- [64] C. Ryan, V. Briganti, C. Hogan, M. O’Neill, and A. Lunghi, *arXiv preprint arXiv:2504.18254* (2025).
- [65] M. J. Graham, C.-J. Yu, M. D. Krzyaniak, M. R. Wasielewski, and D. E. Freedman, *Journal of the American Chemical Society* **139**, 3196 (2017).
- [66] R. Mirzoyan, N. P. Kazmierczak, and R. G. Hadt, *Chemistry—A European Journal* **27**, 9482 (2021).
- [67] C. J. Wedge, G. Timco, E. Spielberg, R. George, F. Tuna, S. Rigby, E. McInnes, R. Winpenny, S. Blundell, and A. Ardavan, *Physical review letters* **108**, 107204 (2012).
- [68] R. H. Lavroff, D. L. Pennington, A. S. Hua, B. Y. Li, J. A. Williams, and A. N. Alexandrova, *Journal of Physical Chemistry Letters* **12**, 10742 (2021).
- [69] E. Salvadori, J. D. Breeze, K.-J. Tan, J. Sathian, B. Richards, M. W. Fung, G. Wolfowicz, M. Oxborrow, N. M. Alford, and C. W. M. Kay, *Scientific Reports* **7**, 41836 (2017).
- [70] S. L. Bayliss, P. Deb, D. W. Laorenza, M. Onizhuk, G. Galli, D. E. Freedman, and D. D. Awschalom, *Physical Review X* **12**, 031028 (2022).
- [71] P. Falcaro, R. Ricco, C. M. Doherty, K. Liang, A. J. Hill, and M. J. Styles, *Chemical Society Reviews* **43**, 5513 (2014).
- [72] T. Yamabayashi, M. Atzori, L. Tesi, G. Cosquer, F. Santanni, M.-E. Boulon, E. Morra, S. Benci, R. Torre, M. Chiesa, *et al.*, *Journal of the American Chemical Society* **140**, 12090 (2018).
- [73] A. Yamauchi, S. Fujiwara, N. Kimizuka, M. Asada, M. Fujiwara, T. Nakamura, and N. Yanai, (2022).